



# A square-lattice D-shaped photonic crystal fiber sensor based on SPR to detect analytes with large refractive indexes

Wei Liu<sup>a</sup>, Chunjie Hu<sup>b</sup>, Lei Zhou<sup>c</sup>, Zao Yi<sup>d</sup>, Chao Liu<sup>a,\*</sup>, Jingwei Lv<sup>a</sup>, Lin Yang<sup>a</sup>, Paul K. Chu<sup>e</sup>

<sup>a</sup> School of Physics and Electronic Engineering, Northeast Petroleum University, Daqing, 163318, PR China

<sup>b</sup> Department of Gynaecology and Obstetrics, The Fourth Affiliated Hospital of Harbin Medical University, Harbin, 150001, China

<sup>c</sup> Department of Orthopedics, The Second Affiliated Hospital of Harbin Medical University, Harbin, 150081, China

<sup>d</sup> Joint Laboratory for Extreme Conditions Matter Properties, Southwest University of Science and Technology, Mianyang, 621010, China

<sup>e</sup> Department of Physics and Department of Materials Science and Engineering, City University of Hong Kong, Tat Chee Avenue, Kowloon, Hong Kong, China

## ARTICLE INFO

### Keywords:

PCF-SPR sensor  
Detecting large RI analytes  
Near-infrared  
Ultra-high sensitivity  
Indium tin oxide (ITO)  
Biochemical safety

## ABSTRACT

With the booming of nanotechnology, surface plasmon resonance (SPR) technology has become one of the most active research hotspots in optical sensing. In this work, a square-lattice photonic crystal fiber (PCF) sensor based-SPR with indium tin oxide (ITO) coating is investigated to detect analytes with large refractive indexes (RIs) varying from 1.380 to 1.405. To confirm the dependence of sensing characteristics on the geometrical parameters, the finite element method (FEM) is applied to modeling and numerical simulation. The big air holes in cladding cause a birefringence effect, which is stronger with y-polarization mode. In this way, the maximum and average spectral sensitivity of 60,000 and 18,400 nm/RIU can be achieved with resolution in  $10^{-6}$  order. Furthermore, this sensor which provides a high-sensitivity detection in large analyte RIs with near-infrared region (1500–2800 nm) shows excellent figure of merit (FOM), signal-to-noise ratio (SNR) and detection limit (DL). There will be more extensive space and prospect for progression in biochemical safety with DNA hybridization, blood glucose analysis and organic chemical samples detection involved.

## 1. Introduction

Surface plasmon resonance (SPR) technique has become a focus due to its non-invasiveness, real-time as well as label-free monitoring [1–3] in refractive index (RI) sensing. In essence, SPR is a critical physical–optical phenomenon involving excitation of electron density oscillations at metal–dielectric interfaces under the irradiation of p-polarized light waves [4]. Furthermore, in SPR excitation, the energy of the incident light is absorbed by the surface plasmon wave (SPW) at the metal–dielectric interfaces, then an obvious resonant peak appears which is sensitive to slight variations in the surroundings. Since the propagation constant of the surface plasmon wave is mainly related to the refractive index of the analyte, SPR is a powerful technique to monitor analytes in real time [5,6]. The advantages of sensors are strong ability to adapt to harsh environment, affordable for mass production, stability and reliability. Consequently, the sensors based on SPR possess sparkling development prospects in environmental monitoring, chemical safety control, biomedical diagnostics, gas and liquid detection, etc [7–9]. The conventional SPR-sensing platforms are based on the prism

coupling [10], slot waveguide [11], and fiber Bragg grating [12], which are costly and bulky. Nevertheless, SPR sensors based optical fiber towardly remedy above drawbacks to provide miniaturized structures and remote sensing [13,14]. In contrast to ordinary optical fiber, photonic crystal fiber (PCF) is especially desirable by virtue of the flexible multi-parameter functionality, portability, large effective area, high nonlinearity and endless single-mode [15,16].

In order to improve the performance of sensors, the choice of plasmonic materials and position of coatings are significant. To date, plentiful plasmonic materials have been mentioned in existing literatures to induce SPR. In particular, silver, copper, aluminum and gold are uniquely favored [17,18]. Silver can offer sharper resonant peak, however, the high oxidization properties obstruct its widespread applications in the aqueous environment. Copper and aluminium suffer from the same problem. Besides, the electrical conductivity of gold is inferior to that of silver and hampered to excite SPR. With the emergence of novel plasmonic materials, indium tin oxide (ITO) comes into sight and has been paid much attention. It has preponderance of anti-oxidation, low cost, and can control the operating wavelength in the

\* Corresponding author.

E-mail address: [mzm-liu@126.com](mailto:mzm-liu@126.com) (C. Liu).

<https://doi.org/10.1016/j.physe.2021.115106>

Received 4 May 2021; Received in revised form 19 November 2021; Accepted 2 December 2021

Available online 4 December 2021

1386-9477/© 2021 Elsevier B.V. All rights reserved.

near-infrared range [19,20]. This greatly overcomes troubles of conventional metal materials.

Furthermore, diverse types of PCF structures have emerged such as internal air holes coated [21,22], nanowires filling [23], external cladding coated [24,25], and D-shaped structures [26]. However, internal air holes coated or nanowires filling are incredibly hard to be achieved. As the surface polishing technology continues to mature, the D-shaped PCF sensing structures are charming. Compared with the entire cladding coated, it can availably reduce the coating area to save economic cost. In addition, the width of plasmonic film can be precisely controlled depending on the location of the fiber core. Therefore, there is a better SPR effect to generate between free electrons and photons, which makes efficient sensing possible.

In view of the above, multifarious PCF-SPR sensors with D-shaped structures and ITO films coated have been designed and investigated successively. Huang [27] suggested a plasmonic sensor which displayed a maximum spectral sensitivity of 6000 nm/RIU with RIs of analyte between 1.28 and 1.34. Dash et al. [28] studied a side-polished PCF sensor based on SPR. An optimal spectral sensitivity of 17,000 nm/RIU, and resolution of  $1.67 \times 10^{-6}$  RIU were acquired when analyte RIs changed from 1.330 to 1.350. Yang et al. [29] reported a concave-shaped PCF-SPR sensor to detect RIs between 1.19 and 1.29 with spectral sensitivity of 1700–10700 nm/RIU. Nevertheless, these PCF-SPR sensors are only suitable for analyte RIs less than 1.38 and analytes with larger RIs in biochemical field are difficult to be differentiated. The sensitivity is a key factor to gauge the performance of a sensor as it reflects the degree of SPW dependence on RI variations in the surroundings, however, the sensitivities of the aforementioned sensors are less than 20,000 nm/RIU and not satisfactory. Therefore, in order to expand the applications for analytes with large RIs, it is imperative to design better sensors.

Herein, a high-sensitivity D-shaped PCF-SPR sensor with ITO coating is designed to achieve the detection for large RI analytes in the near-infrared range. By optimizing the structural parameters including the size, space, position of air holes, as well as thickness and width of the ITO film, a spectral sensitivity of 60,000 nm/RIU, average sensitivity of 18,400 nm/RIU, and homologous resolution of  $1.67 \times 10^{-6}$  RIU can be obtained for the analyte RIs from 1.380 to 1.405 with operational wavelength between 1500 nm and 2800 nm.

## 2. Structural design and numerical simulation

The cross-sectional schematic of the recommended D-shaped PCF-SPR sensor with the ITO coated is illustrated in Fig. 1(a). This structure has a square lattice with four different air holes and the external cladding can be prepared by side polishing technique, which is convenient for metal films to be coated. Fused silica is selected as background material. Due to cheaper than gold or silver, indium tin oxide (ITO) is selected the plasmonic film to control the working wavelength in near-infrared range. The fabrication procedure is a crucial matter in any design. The proposed D-shaped PCF can be practically fabricated such as the standard stack-and-draw, tube stacking drilling and sol-gel methods [30,31]. In this work, stack-and-draw technique is adopted as shown in Fig. 1(b). Different thickness glass tubes can be obtained by stacking solid rods and capillaries together and stretching them at a certain rate. Combined with polishing and chemical deposition technology, ITO film can be coated on the D-shaped PCF surface [18]. The optimal parameters of the sensor are as follows - air hole diameters are  $d_1 = 1.0 \mu\text{m}$ ,  $d_2 = 1.8 \mu\text{m}$ ,  $d_3 = 2.4 \mu\text{m}$ , and  $d_4 = 2.8 \mu\text{m}$ ; pitch of two central big holes is  $\Lambda = 7.0 \mu\text{m}$ ; distance from the center of the largest air hole is  $D = 3.5 \mu\text{m}$ ; thickness, width of ITO and height are  $T = 70 \text{ nm}$ ,  $L = 8.0 \mu\text{m}$ , and  $H = 5.2 \mu\text{m}$ . The RI of air is  $n = 1.0$  and the background material RI of fused silica is defined by Sellmeier equation [32,33]:

$$n(\lambda) = \sqrt{\left(1 + \frac{B_1\lambda^2}{\lambda^2 - C_1} + \frac{B_2\lambda^2}{\lambda^2 - C_2} + \frac{B_3\lambda^2}{\lambda^2 - C_3}\right)}, \quad (1)$$

where  $n$  and  $\lambda$  represents the RI of fused silica and operating wavelength of the incident light, respectively, and  $B_1 = 0.6916663$ ,  $B_2 = 0.407934$ ,  $B_3 = 0.897479$ ,  $C_1 = 0.004679$ ,  $C_2 = 0.013512$  and  $C_3 = 97.934003$  are the Sellmeier coefficients. The permittivity of ITO deposited on the PCF can be calculated by the following equation [20,34]:

$$\varepsilon(\omega) = \varepsilon - \frac{\omega_p^2}{\omega^2 + i\omega\Gamma}, \quad (2)$$

where  $\varepsilon$  is intraband dielectric constant,  $\Gamma = 0.111 \text{ eV}$  is the damping coefficient, and  $\omega_p = 2.19 \text{ eV}$ . Eq. (2) is based on Drude model.

The finite element method (FEM) based on COMSOL software is utilized to study the sensing performance of the D-shaped PCF-SPR sensor [35]. During our research, a circular perfectly matched layer (C-PML) as absorbing boundary condition is established by two-dimensional modeling, which is engaged to dwindle unnecessary

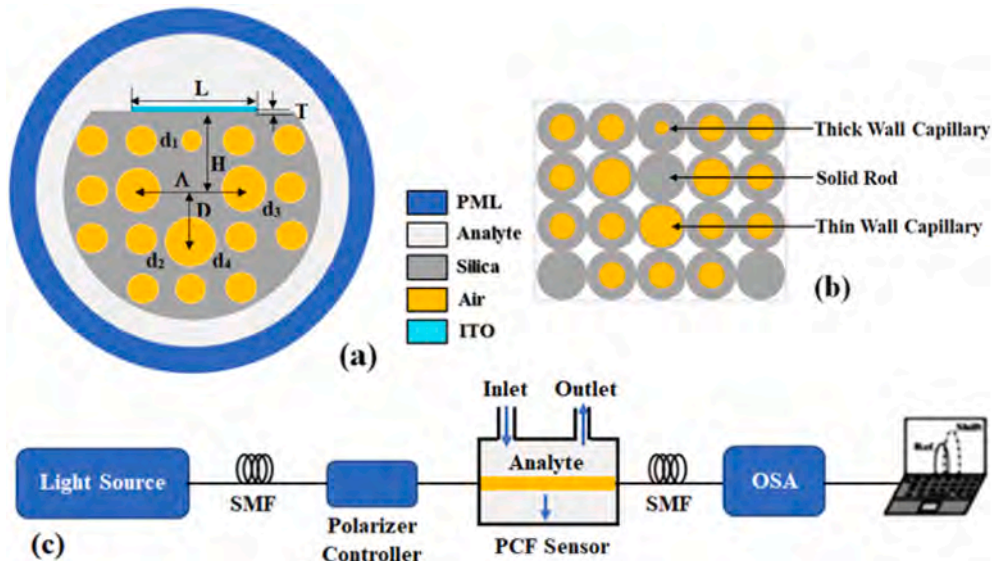


Fig. 1. (a) Cross-sectional view of the D-shaped PCF-SPR sensor; (b) The stacked preform of presented PCF; (c) The schematic of recommended SPR setup.

electromagnetic reflection [36]. Virtually, the C-PML domain function is used for steady-state control equation. For a mode with certain operating frequency, light can be absolutely confined inside the fiber core to propagate. In the simulation process, the convergence tests are carried out by optimizing the mesh size and C-PML thickness to produce more accurate results. The computational area is divided by ultra-refined triangular grid, which contains 14,642 domain units and 1079 boundary units. This precise and detailed division makes it easier to identify suitable modes. The energy can be infiltrated from the core to cladding territory because the finite number of air cavities for the PCF is considered as the confinement loss (CL), which can be stated by the equation as follows [37,38]:

$$L_c \left( \text{dB} / \text{cm} \right) = 40\pi \times \frac{\text{Im}(n_{\text{eff}})}{\ln(10)\lambda} \times 10^4, \quad (3)$$

where  $\lambda$  stands for the wavelength of free space and  $\text{Im}[n_{\text{eff}}]$  is the imaginary part of the refractive index. Excitation of surface plasmon is characterized by calculating the confinement loss of the optical fiber and the set-up is presented in Fig. 1(b). Wideband light is emitted by the laser through a single-mode fiber to irradiate the D-shaped PCF. When the analyte RIs are changed due to adsorbate species, phase matching of the core-guided mode and SPP mode is affected consequently producing blue-shift or red-shift that is monitored by an optical spectrum analyzer (OSA) and analyzed by a computer.

### 3. Results and discussion

Fig. 2(A) describes the confinement loss and electric field distribution of the x- and y-polarization modes with the analyte RIs varying from 1.380 to 1.385. Compared to the x-polarization mode, the CL increases first and then decreases for y-polarization mode with the wavelength increasing [39,40]. When the analyte RIs are changed from 1.380 to 1.385, there is a horizontal shift for CL peaks. In comparison, the x-polarization mode will not appear. From the perspective of electric field distribution, in the y-polarization mode, more energy is transferred from the core to ITO film surface to produce stronger coupling effect. Therefore, in the subsequent analysis, the y-polarization mode is selected to evaluate the characteristics of the D-shaped PCF-SPR sensor.

The dispersion relations of the SPP mode, core-guided mode, and CL with dependence on wavelength are visually presented in Fig. 2(B). The distribution of three electric fields reveals that the majority of the energy is concentrated on the core (inset (a)) and ITO film surface (inset (b)) resulting in energy coupling between them (inset (c)). The real parts of the effective indexes of the core-guided mode and SPP mode are shown as orange and blue lines, respectively. As the wavelength increases gradually,  $\text{Re}(n_{\text{eff}})$  of two modes decreases at different rates and both have the same  $\text{Re}(n_{\text{eff}})$  at 2310 nm. The relationship between the CL and wavelength is indicated by the purple line and the maximum loss peak appears at the intersection of the two curves. The results show that the two modes satisfy the phase matching conditions to generate SPR effect. The resonant wavelength of the PCF-based SPR sensor is sensitive to

the structural parameters and the effects are investigated for the analyte RI of  $n_a = 1.380$ . The dependence of the CL spectra on resonant wavelength with different air holes is shown in Fig. 3. With the  $d_1$  increasing, the offset in the CL peaks is quite small and hardly changes, indicating that the change of  $d_1$  has little effect on light transmission from fiber core to ITO layer. When  $d_2$  is changed from 1.4  $\mu\text{m}$  to 1.8  $\mu\text{m}$ , the CL peaks show an upward trend and become sharper. It is explained that a larger  $d_2$  can reduce the effective RI difference between cladding and core, and enables more incident light to propagate in the core.

As  $d_3$  is increased to  $d_4$ , the coupling effect between the core-guided mode and SPP mode becomes worse and the CL peaks decrease gradually. According to the longitudinal offset of the CL peaks, the variation of air holes  $d_3$  has a greater impact on energy transmission. The reason is that the smaller air holes near the core is, the more convenient it is for the energy to obtain a larger storage space, and there will be more energy transferred to metal surface to produce resonant effect. Thus, the optimal air holes parameters are selected as follows:  $d_1 = 1.0 \mu\text{m}$ ,  $d_2 = 1.8 \mu\text{m}$ ,  $d_3 = 2.4 \mu\text{m}$ , and  $d_4 = 2.8 \mu\text{m}$ .

Fig. 4 (a)-(c) exhibit the CL spectra for different values of pitch  $\Lambda$  between  $d_3$ , distance  $d_4$  from the center  $D$ , and height of ITO film away from center  $H$ , respectively. As shown in Fig. 4(a), the resonant peaks ascend by degrees when  $\Lambda$  changes from 6.2  $\mu\text{m}$  to 7.0  $\mu\text{m}$ . Coupling between the core-guided mode and SPP mode will occur by modulating the distance between the large air holes ( $d_3$ ) on both sides of the fiber core. Therefore, a larger  $\Lambda$  provides more space for energy to focus on the core. Fig. 4(b) illustrates the effects of different  $D$  values on CL peaks, which is the largest for  $D = 3.5 \mu\text{m}$ . This indicates that phase matching of the two modes is improved with  $D$  increasing. Further analysis shows that a larger  $D$  increases the mode field area and contributes to the energy distribution in the fiber core. When  $H$  is between 5.2  $\mu\text{m}$  and 5.6  $\mu\text{m}$ , the dependence of the CL spectra on wavelength is reflected in Fig. 4 (c). With  $H$  values enlarging, the CL peaks decrease gradually. It shows that a smaller  $H$  is more beneficial to the energy to be transferred from fiber core to ITO film surface, so that phase matching conditions can be better satisfied. The reason is that when the polishing surface is lower and closer to the fiber core, it is more convenient for the incident light to propagate between fiber core and ITO film. As a result, the two modes can stimulate each other to produce stronger resonant effect.

Fig. 5(a) and (b) present the variations in the CL spectra for different ITO film thicknesses and widths, respectively. As shown in Fig. 5(a), when the thickness of the ITO film ( $T$ ) increases from 70 nm to 90 nm, the CL peaks decrease gradually and also widen, in addition to a red-shift in the CL spectra, which is attributed to that the  $\text{Re}(n_{\text{eff}})$  of the core-guided mode is nearly unchanged, while the  $\text{Re}(n_{\text{eff}})$  of SPP mode increases. Thus, it is indicated that a thinner ITO film is more favorable to the energy of fiber core to reduce damping and facilitate energy transfer to produce a strong coupling effect. The relationship between the CL and wavelength is shown in Fig. 5(b) for different ITO film widths ( $L$ ). As the width increases, the resonant effect weakens and the CL peaks decrease. This manifests that an excessively large width limits the energy transmission from core to ITO film surface. Therefore, it is no need to deposit

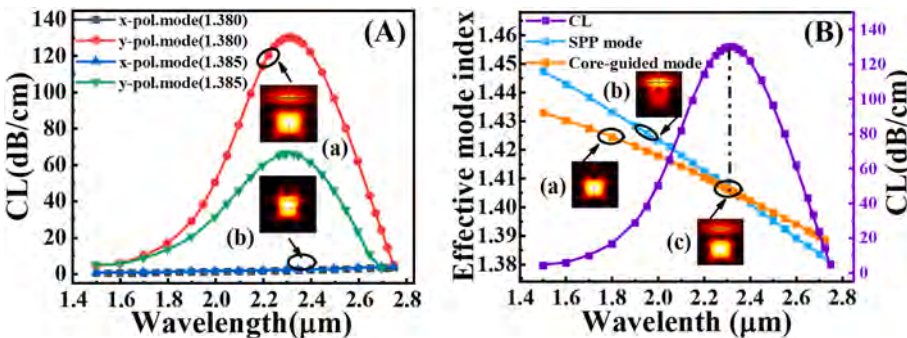


Fig. 2. (A) CL and electric field distribution of the x-polarization mode and y-polarization mode for analyte RIs of 1.380–1.385; (B) Dispersion relations of the SPP mode (blue), core-guided mode (orange), and confinement loss (purple) with wavelength dependence ( $n_{\text{air}} = 1$ ,  $n_{\text{ana}} = 1.38$ ,  $d_1 = 1.0 \mu\text{m}$ ,  $d_2 = 1.8 \mu\text{m}$ ,  $d_3 = 2.4 \mu\text{m}$ ,  $d_4 = 2.8 \mu\text{m}$ ,  $\Lambda = 7.0 \mu\text{m}$ ,  $D = 3.5 \mu\text{m}$ ,  $T = 70 \text{ nm}$ ,  $L = 8.0 \mu\text{m}$ , and  $H = 5.2 \mu\text{m}$ ). (For interpretation of the references to colour in this figure legend, the reader is referred to the Web version of this article.)

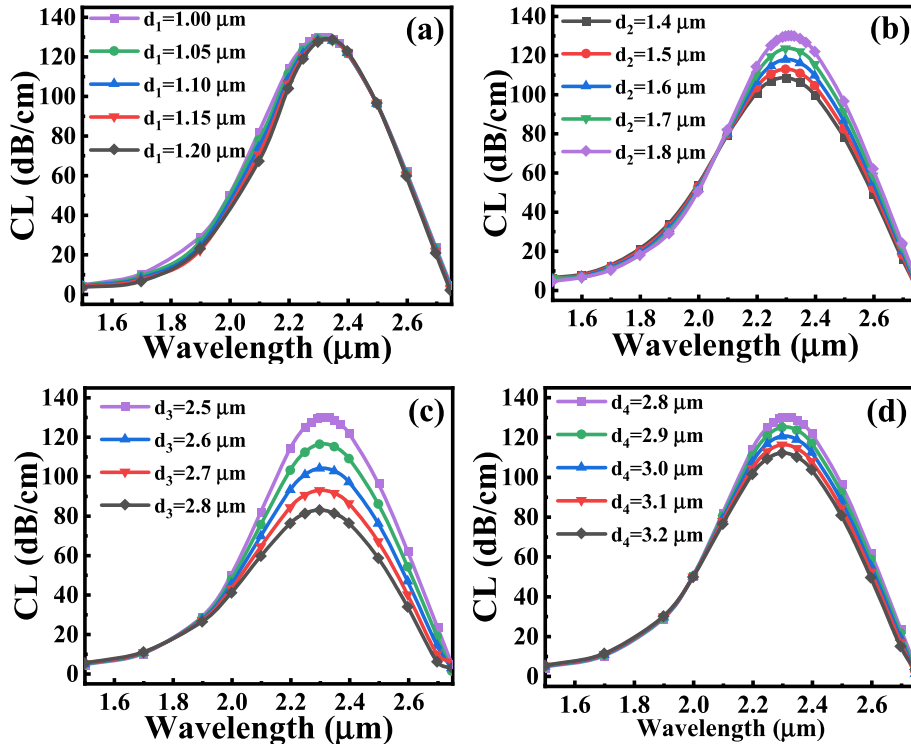


Fig. 3. CL spectra of the sensor for different air holes diameters: (a)  $d_1$ , (b)  $d_2$ , (c)  $d_3$ , and (d)  $d_4$  ( $n_{\text{air}} = 1$ ,  $n_{\text{ana}} = 1.38$ ,  $d_1 = 1.0 \mu\text{m}$ ,  $d_2 = 1.8 \mu\text{m}$ ,  $d_3 = 2.4 \mu\text{m}$ ,  $d_4 = 2.8 \mu\text{m}$ ,  $\Lambda = 7.0 \mu\text{m}$ ,  $D = 3.5 \mu\text{m}$ ,  $T = 70 \text{ nm}$ ,  $L = 8.0 \mu\text{m}$ , and  $H = 5.2 \mu\text{m}$ ).

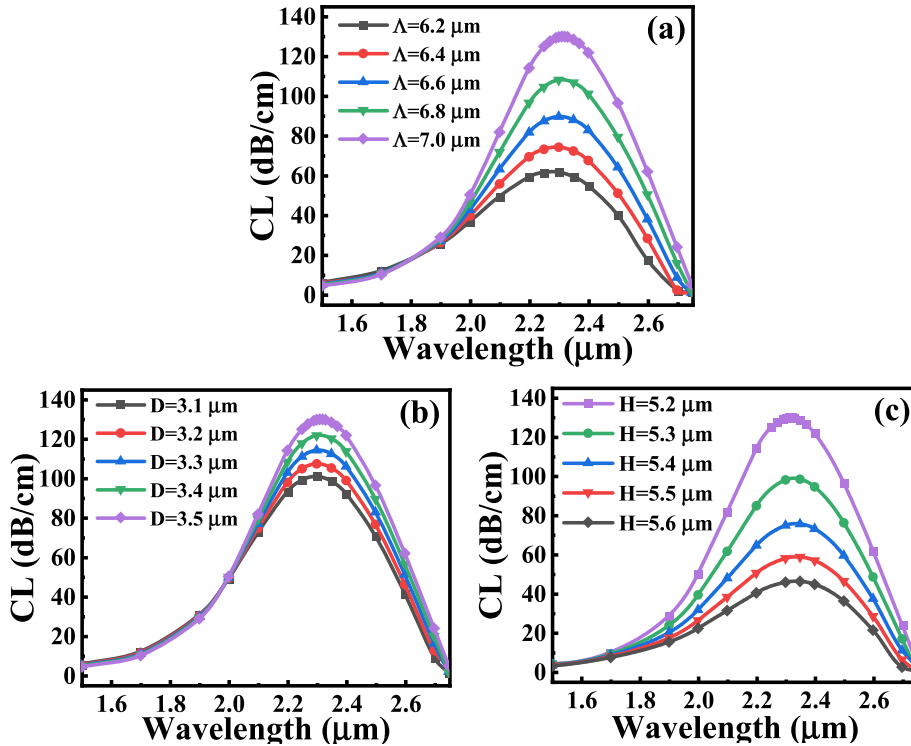


Fig. 4. CL spectra variation: (a) Pitch  $\Lambda$  between  $d_3$ , (b) Distance  $d_4$  from the center  $D$ , and (c) Height of ITO film away from center  $H$  ( $n_{\text{air}} = 1$ ,  $n_{\text{ana}} = 1.38$ ,  $d_1 = 1.0 \mu\text{m}$ ,  $d_2 = 1.8 \mu\text{m}$ ,  $d_3 = 2.4 \mu\text{m}$ ,  $d_4 = 2.8 \mu\text{m}$ ,  $\Lambda = 7.0 \mu\text{m}$ ,  $D = 3.5 \mu\text{m}$ ,  $T = 70 \text{ nm}$ ,  $L = 8.0 \mu\text{m}$ , and  $H = 5.2 \mu\text{m}$ ).

the plasmonic sensing materials on the whole D-shaped platform, only need to deposit a part of the length according to the location of the core. This can save the fabrication cost and prompt resonant effect to reach the best state.

SPR is sensitive to tiny RI variations near the surroundings (analytes). Because  $\text{Re}(n_{\text{eff}})$  of the SPP mode depends on the analyte RIs, a small variation for analyte RI will change  $\text{Re}(n_{\text{eff}})$  of the SPP mode and resonant wavelength. The proposed PCF-SPR sensor can effectively

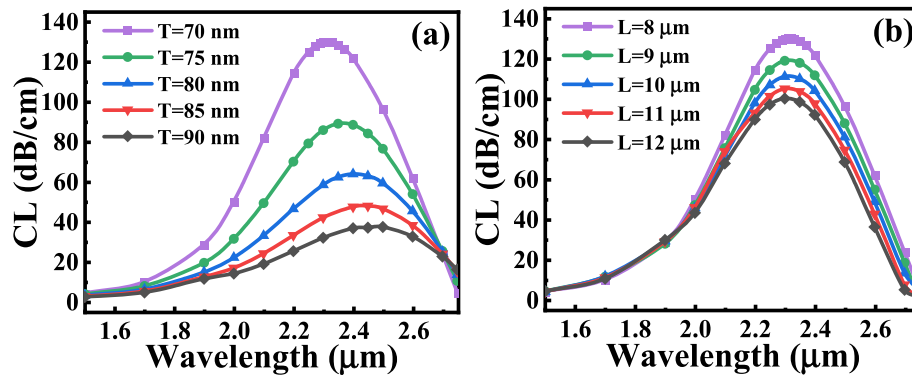


Fig. 5. The variations of CL spectra with different ITO film (a) thicknesses ( $T$ ) and (b) widths ( $L$ ) ( $n_{\text{air}} = 1$ ,  $n_{\text{ana}} = 1.38$ ,  $d_1 = 1.0 \mu\text{m}$ ,  $d_2 = 1.8 \mu\text{m}$ ,  $d_3 = 2.4 \mu\text{m}$ ,  $d_4 = 2.8 \mu\text{m}$ ,  $\Lambda = 7.0 \mu\text{m}$ ,  $D = 3.5 \mu\text{m}$ ,  $T = 70 \text{ nm}$ ,  $L = 8.0 \mu\text{m}$ , and  $H = 5.2 \mu\text{m}$ ).

monitor high RI analytes. In general, the lower limit of RI detection greater than 1.33 is referred to high RI sensing, which can be applied to biomedical and chemical safety fields such as DNA hybridization, blood glucose analysis and organic chemical samples detection [41–43].

The CL spectra for the variations of analyte RIs from 1.380 to 1.405 are shown in Fig. 6(a), and the resonant wavelength shows a blue-shift. As shown in Fig. 2(b), the curve slope for  $\text{Re}(n_{\text{eff}})$  of the SPP mode is larger than that of the core-guided mode. With the analyte RIs increasing, the position of curve representing the  $\text{Re}(n_{\text{eff}})$  of core-guided mode is almost unchanged, while the position of the curve representing  $\text{Re}(n_{\text{eff}})$  of the SPP mode gradually moves towards to the short wavelength direction, resulting in a blue shift for the intersection of the two curves under each RI. Since the intersection of two modes refers to the phase matching point, the corresponding positions are resonant wavelength and resonant peak. Therefore, with the increase of analyte RIs, the resonant wavelength and resonant peak also exhibit a trend of blue shift [5]. Fig. 6(c–h) shows the distribution of energy fields under the different resonant wavelengths when the analyte RIs change from 1.380 to 1.405. It is indicated that the energy transmission is the largest and the resonance between two modes is the strongest with the RI analyte of 1.380. However, in combination with Fig. 6(a), when the analyte RIs change from 1.380 to 1.385, the offset of the resonant wavelength is the smallest and sensitivity is the lowest.

The sensitivity is calculated by the wavelength interrogation method as shown below [44]:

$$S_{\lambda} (\text{nmRIU}^{-1}) = \Delta\lambda_{\text{peak}} / \Delta n_a, \quad (4)$$

where  $\Delta\lambda_{\text{peak}}$  is the shift of the resonant peak position and  $\Delta n_a$  is the variation of adjacent analyte RIs (0.005). For RI variations from 1.380 to 1.385, 1.385 to 1.390, 1.390 to 1.395, 1.395 to 1.400, and 1.400 to 1.405, the changes in the resonant wavelength are 10 nm, 20 nm, 50 nm, 80 nm, and 300 nm and the corresponding wavelength sensitivities are 2000 nm/RIU, 4000 nm/RIU, 10,000 nm/RIU, 16,000 nm/RIU and 60,000 nm/RIU as shown in Fig. 6(b). The proposed D-shaped PCF-SPR sensor exhibits a maximum spectral sensitivity of 60,000 nm/RIU and average sensitivity of 18,400 nm/RIU.

Supposing that the minimum wavelength resolution is  $\Delta\lambda_{\text{min}} = 0.1 \text{ nm}$ , the analyte RI resolution of the sensor can be calculated by Ref. [45]:

$$R(\text{RIU}) = \Delta n_a \times \Delta\lambda_{\text{min}} / \Delta\lambda_{\text{peak}}, \quad (5)$$

The results shows that a maximum RI resolution of proposed sensor is  $1.67 \times 10^{-6} \text{ RIU}$  for analyte RIs between 1.400 and 1.405. Additionally, polynomial fit of the resonant wavelengths with analyte RIs in Fig. 7(a) reveal an R-square value of 0.99213 and Fig. 7(b) shows the histogram

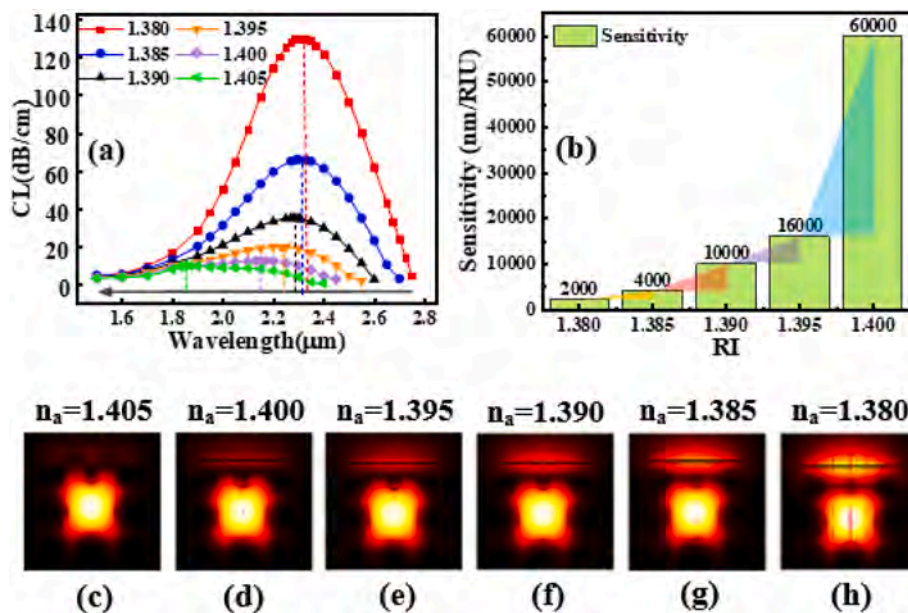


Fig. 6. (a) CL spectra of the sensor for different analyte RIs; (b) The dependence of sensitivity on analyte RIs; (c–h) Energy field distribution of analyte RIs from 1.380 to 1.405 in the resonant wavelengths ( $n_{\text{air}} = 1$ ,  $d_1 = 1.0 \mu\text{m}$ ,  $d_2 = 1.8 \mu\text{m}$ ,  $d_3 = 2.4 \mu\text{m}$ ,  $d_4 = 2.8 \mu\text{m}$ ,  $\Lambda = 7.0 \mu\text{m}$ ,  $D = 3.5 \mu\text{m}$ ,  $T = 70 \text{ nm}$ ,  $L = 8.0 \mu\text{m}$ , and  $H = 5.2 \mu\text{m}$ ).

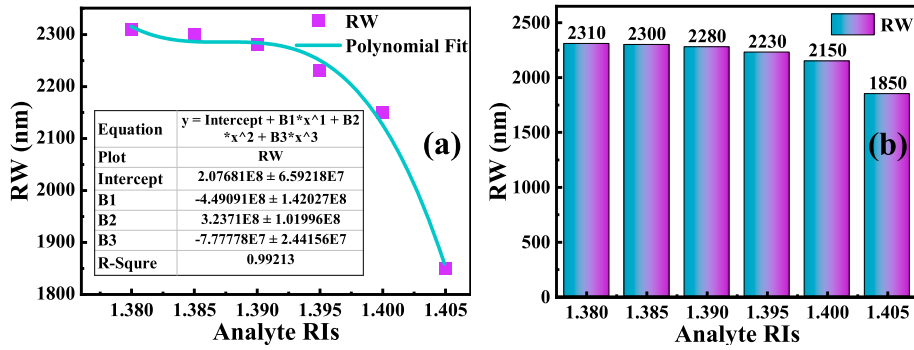


Fig. 7. The variations of RW with different analyte RIs: (a) Polynomial fit and (b) Histogram distributions.

distributions between resonant wavelengths and analyte RIs.

Besides the sensitivity, the figure of merit (FOM), signal-to-noise ratio (SNR), and detection limit (DL) are derived according to the following relationships [46]:

$$FOM = \frac{S_\lambda}{FWHM} \quad (6)$$

$$SNR = \frac{\Delta\lambda_{res}}{FWHM} \quad (7)$$

$$DL = \frac{FWHM}{1.5(SNR)^{0.25}}, \quad (8)$$

where FWHM is the full-width at half-maximum of the CL peak and  $\Delta\lambda_{res}$  represents the variation of the resonant wavelength. The best FOM of  $95.81 \text{ RIU}^{-1}$  and SNR of 0.48 are achieved for an analyte RI of 1.400, and the changes in the FWAM, FOM, SNR and DL of the PCF-SPR sensor are displayed in Fig. 8 (a)-(d). In addition, the variations of the resonant wavelength ( $\Delta\lambda_{res}$ ), spectral sensitivity, resolution, FWHM, FOM, SNR, and DL for the analyte RIs range of 1.380–1.405 are summarized in Table 1, which better illustrates extraordinary sensing characteristics of the recommended sensor.

Table 2 compares the optical properties of PCF-SPR sensors recently studied. The choice of plasmonic materials is very important to the sensing performance. The table lists a series of sensors with conventional gold, silver, copper and aluminum, as well as novel ITO materials as the sensing layers coated on the surface of the PCF. Compared with the previously proposed sensors, this sensor can detect large RI analytes in a wider near-infrared wavelength region with higher sensitivity. Therefore, the proposed sensor can be applied in chemical safety and biomedical detection fields, displaying greater advantages and inestimable potentials.

#### 4. Conclusion

In summary, the novel PCF-SPR sensor is proposed and investigated in near-infrared region, and large RIs detection and high sensitivity are obtained. To improve the coupling strength between the core-guided mode and SPP mode, the D-shaped structure is adopted and analyzed by FEM and C-PML methods. Moreover, ITO is selected as the plasmonic sensing material to control the operating wavelength within 1500 nm–2800 nm. Our analysis reveals a maximum spectral sensitivity of 60,000 nm/RIU, average spectral sensitivity of 18,400 nm/RIU and corresponding resolution of  $1.67 \times 10^{-6} \text{ RIU}$  with analyte RIs varying

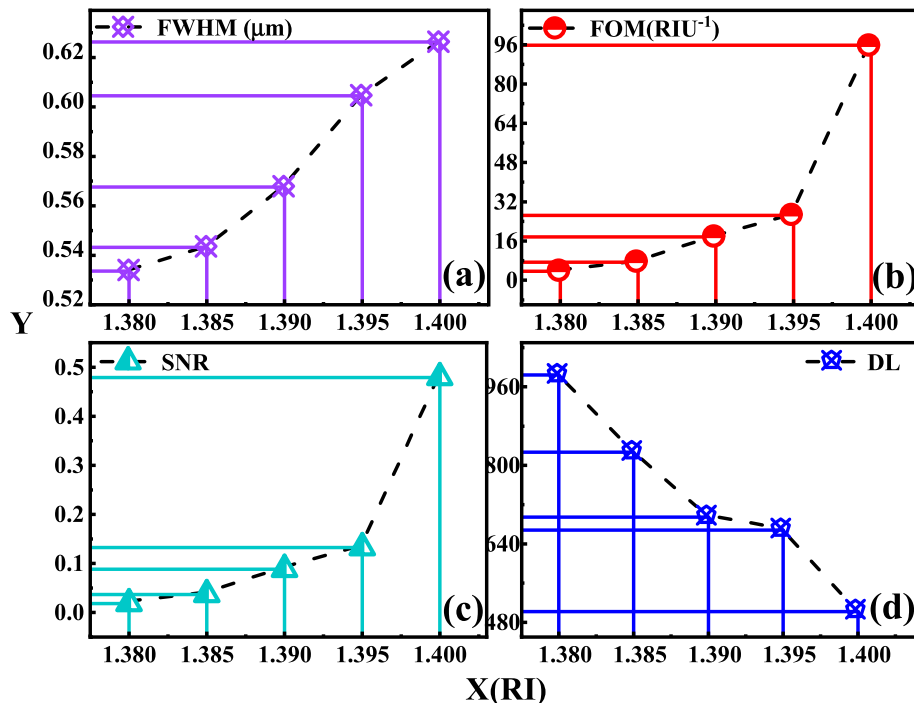


Fig. 8. Properties of the PCF-SPR sensor: (a) FWHM, (b) FOM, and (c) SNR, (d) DL.



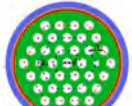





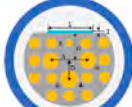
**Table 1**

Properties of the sensor for different analyte RIs.

Analyte RI	$\Delta\lambda_{res}$ (nm)	Sensitivity (nm/RIU)	Resolution (RIU <sup>-1</sup> )	FWHM	FOM (RIU <sup>-1</sup> )	SNR	Detection limit
1.380	10	2000	$5.00 \times 10^{-5}$	0.5436	3.68	0.02	984.12
1.385	20	4000	$2.50 \times 10^{-5}$	0.5432	7.36	0.04	826.78
1.390	50	10,000	$1.00 \times 10^{-6}$	0.5676	17.62	0.09	694.60
1.395	80	16,000	$6.25 \times 10^{-6}$	0.6045	26.47	0.13	668.16
1.400	300	60,000	$1.67 \times 10^{-6}$	0.6263	95.81	0.48	501.84

**Table 2**

Performance comparisons with recently reported sensors.

Ref.	Characteristics	Wav. range (nm)	RI range	Sens. (nm/RIU)	Str. diagram
[47]	Gold-deposited D-shaped sensor	1400–1800	1.36–1.38	3340	
[48]	Silver-continuous grating sensor	505–793	1.33–1.36	13,600	
[49]	Copper-based SPR biosensor	530–780	1.33–1.37	2000	
[50]	Aluminium-coated PCF-SPR sensor	1700–2000	1.32–1.34	5000	
[27]	ITO-layer plasmonic sensor	1300–2100	1.28–1.34	6000	
[16]	PCF sensor with ITO coatings	1200–2250	1.22–1.33	15,000	
[19]	SPR sensor with ITO coated in holes	1370–1650	1.33–1.35	2000	
[51]	PCF-SPR sensor with ITO coated externally	1380–2260	1.26–1.38	35,000	
This work	High-sensitive sensor detecting large RIs	1500–2800	1.38–1.405	60,000	

from 1.380 to 1.405. This unique structure has important technical significance and application potentials for the detection of high RI substances in chemical safety and biomedical monitoring fields.

#### Declaration of competing interest

The authors declare no conflicts of interest.

#### Acknowledgments

This work was jointly supported by and Local Universities Reformation and Development Personnel Training Supporting Project from Central Authorities [140119001], City University of Hong Kong Strategic Research Grant (SRG) [grant numbers 7005105 and 7005265], and Scientific Research Fund of Sichuan Province Science and Technology Department [2020YJ0137].

## References

- [1] C.G. Li, B. Yan, J.J. Liu, Refractive index sensing characteristics in a D-shaped photonic quasi-crystal fiber sensor based on surface plasmon resonance, *J. Opt. Soc. Am. A* 36 (10) (2019) 1663–1668.
- [2] H.X. Han, D.L. Hou, L. Zhao, N.N. Luan, L. Song, Z.H. Liu, Y.D. Lian, J.F. Liu, Y. S. Hu, A large detection-range plasmonic sensor based on an H-shaped photonic crystal fiber, *Sensors* 20 (4) (2020) 1009–1016.
- [3] M.B. Hossain, T.V. Mahendiran, L.F. Abdulrazak, I.M. Mehedi, M.M. Rana, Numerical analysis of gold coating based quasi D-shape dual core PCF SPR sensor, *Opt. Quant. Electron.* 52 (10) (2020) 446–458.
- [4] C. Liu, J.W. Lv, W. Liu, F.M. Wang, P.K. Chu, Overview of refractive index sensors comprising photonic crystal fibers based on the surface plasmon resonance effect, *Chin. Opt. Lett.* 19 (10) (2021) 102202.
- [5] J.W. Wang, C. Liu, F.M. Wang, W.Q. Su, L. Yang, J.W. Lv, G.L. Fu, X.L. Li, Q. Liu, T. Sun, P.K. Chu, Surface plasmon resonance sensor based on coupling effects of dual photonic crystal fibers for low refractive indexes detection, *Results Phys.* 18 (2020) 103240.
- [6] M.S. Islam, J. Sultana, A.A. Rifat, R. Ahmed, A. Dinovitsier, B.W.-H. Ng, H. Ebendorff-Heidepriem, D. Abbott, Dual-polarized highly sensitive plasmonic sensor in the visible to near-IR spectrum, *Opt Express* 26 (23) (2018) 30347–30361.
- [7] M.S. Hossain, S. Sen, M.M. Hossain, Design of a chemical sensing circular photonic crystal fiber with high relative sensitivity and low confinement loss for terahertz (THz) regime, *Optik* 222 (2020) 165359.
- [8] S. Sen, M.A. Shafi, A.S. Sikder, MdS. Hossain, M.M. Azad, Zeonex based decagonal photonic crystal fiber (D-PCF) in the terahertz (THz) band for chemical sensing applications, *Sens. Bio-Sens. Res.* 31 (2021) 100393.
- [9] S. Sen, K. Ahmed, Design of terahertz spectroscopy based optical sensor for chemical detection, *SN Applied Sciences Journal* 1 (10) (2019) 1215.
- [10] E. Kretschmann, H. Raether, Radiative decay of non radiative surface plasmons excited by light, *Ztschrift Für Naturforschung A* 23 (12) (1968) 2135–2136.
- [11] J. Shibayama, K. Shimizu, J. Yamauchi, H. Nakano, Surface plasmon resonance waveguide sensor in the terahertz regime, *J. Lightwave Technol.* 34 (10) (2016) 2518–2525.
- [12] Z.H. Li, Z.Y. Yu, Y.B. Shen, X.K. Ruan, Y.X. Dai, Graphene enhanced leaky mode resonance in tilted fiber bragg grating: a new opportunity for highly sensitive fiber optic sensor, *IEEE Access* 7 (2019) 26641–26651.
- [13] M. Liu, X. Yang, B.Y. Zhao, J.Y. Hou, Square array photonic crystal fiber-based surface plasmon resonance refractive index sensor, *Mod. Phys. Lett. B* 31 (36) (2017) 1750352.
- [14] M.R. Islam, M.A. Jamil, S.A.H. Ahsan, M.M.I. Khan, F. Mehjabin, J.A. Chowdhury, M. Islam, Highly birefringent gold-coated SPR sensor with extremely enhanced amplitude and wavelength sensitivity, *Eur. Phys. J. Plus* 136 (2) (2021) 238–251.
- [15] K. Ahmed, B.K. Paul, M.S. Islam, S. Chowdhury, S. Sen, M.I. Islam, S. Asaduzzaman, Ultra-high birefringence and lower beat length for square shape PCF: analysis effect on rotation angle and eccentricity, *Alex. Eng. J.* 57 (4) (2018) 3683–3691.
- [16] C. Liu, J.W. Wang, F.M. Wang, W.Q. Su, L. Yang, J.W. Lv, G.L. Fu, X.L. Li, Q. Liu, T. Sun, P.K. Chu, Surface plasmon resonance (SPR) infrared sensor based on D-shape photonic crystal fibers with ITO coatings, *Opt Commun.* 464 (2020) 125496.
- [17] Q. Liu, Z. Ma, Q. Wu, W.L. Wang, The biochemical sensor based on liquid-core photonic crystal fiber filled with gold, silver and aluminum, *Opt Laser. Technol.* 130 (2020) 106363.
- [18] A.A. Noman, E. Haque, M.A. Hossain, N.H. Hai, Y. Namihira, F. Ahmed, Sensitivity enhancement of modified D-shaped microchannel PCF-based surface plasmon resonance sensor, *Sensors* 20 (21) (2020) 6049.
- [19] J.N. Dash, R. Jha, SPR biosensor based on polymer PCF coated with conducting metal oxide, *IEEE Photon. Technol. Lett.* 26 (6) (2014) 595–598.
- [20] J.N. Dash, R. Das, SPR based magnetic-field sensing in microchannelled PCF: a numerical approach, *J. Opt.* 20 (11) (2018) 1–11.
- [21] F. Haider, R.A. Aoni, R. Ahmed, G.A. Mahdiraji, M.F. Azman, F.R.M. Adikan, Mode-multiplex plasmonic sensor for multi-analyte detection, *Opt. Lett.* 45 (14) (2020) 3945–3948.
- [22] D.M. Li, W. Zhang, H. Liu, J.F. Hu, G.Y. Zhou, High sensitivity refractive index sensor based on multicoating photonic crystal fiber with surface plasmon resonance at near-Infrared wavelength, *IEEE Photonics J* 9 (2) (2017) 6801608.
- [23] Y. Lu, X.C. Yang, M.T. Wang, J.Q. Yao, Surface plasmon resonance sensor based on hollow-core PCFs filled with silver nanowire, *Electron. Lett.* 51 (21) (2015) 1675–1677.
- [24] M.B. Hossain, S.M.R. Islam, K.M.T. Hossain, L.F. Abdulrazak, M.N. Sakib, I. S. Amiri, High sensitivity hollow core circular shaped PCF surface plasmonic biosensor employing silver coat: a numerical design and analysis with external sensing approach, *Results Phys.* 16 (2020) 102909.
- [25] A. Zelaci, A. Yasli, C. Kalyoncu, H. Ademgil, Generative adversarial neural networks model of photonic crystal fiber based surface plasmon resonance sensor, *J. Lightwave Technol.* 39 (5) (2021) 1515–1522.
- [26] J.P. Chen, S.L. Hou, J.L. Lei, An ultra-sensitive medical sensor for low refractive index analytes, *Jpn. J. Appl. Phys.* 60 (3) (2021), 030908.
- [27] T.Y. Huang, Highly sensitive SPR sensor based on D-shaped photonic crystal fiber coated with indium tin oxide at near-infrared wavelength, *Plasmonics* 12 (3) (2016) 583–588.
- [28] J.N. Dash, R. Jha, Highly sensitive side-polished birefringent PCF-based SPR sensor in near IR, *Plasmonics* 11 (6) (2016) 1505–1509.
- [29] Z. Yang, L. Xia, C. Li, X. Chen, D.M. Liu, A surface plasmon resonance sensor based on concave-shaped photonic crystal fiber for low refractive index detection, *Opt Commun.* 430 (2019) 195–203.
- [30] W. Liu, Y. Shi, Z. Yi, C. Liu, F.M. Wang, X.L. Li, J.W. Lv, L. Yang, P.K. Chu, Surface plasmon resonance chemical sensor composed of a microstructured optical fiber for the detection of an ultra-wide refractive index range and gas-liquid pollutants, *Opt. Express* 29 (25) (2021) 40734–40747.
- [31] M.S. Hossain, M.M. Hasan, S. Sen, M.S.H. Mollah, M.M. Azad, Simulation and analysis of ultra-low material loss of single-mode photonic crystal fiber in terahertz (THz) spectrum for communication applications, *J. Opt. Commun.* 4873 (2021), <https://doi.org/10.1515/joc-2020-0224>.
- [32] C.Y. Li, B.B. Song, Y. Guo, J.X. Wu, W. Huang, X.J. Wu, C. Jin, S.Y. Chen, Two modes excited SPR sensor employing gold-coated photonic crystal fiber based on three-layers air-holes, *IEEE Sensor. J.* 20 (11) (2020) 5893–5899.
- [33] M.I. Islam, B.K. Paul, K. Ahmed, M.R. Hasan, S. Chowdhury, M.S. Islam, S. Sen, A. N. Bahar, S. Asaduzzaman, Highly birefringent single mode spiral shape photonic crystal fiber based sensor for gas sensing applications, *Sens. Bio-Sens. Res.* 14 (2017) 30–38.
- [34] J.P. Maria, M. Losego, D.N. Leonard, B. Laughlin, G. Duscher, Surface plasmon resonance in conducting metal oxides, *J. Appl. Phys.* 100 (5) (2016), 054905.
- [35] F. Haider, R.A. Aoni, R. Ahmed, A.E. Miroshnichenko, Highly amplitude-sensitive photonic crystal fiber based plasmonic sensor, *J. Opt. Soc. Am. B* 35 (11) (2018) 2816–2821.
- [36] K. Ahmed, B.K. Paul, S. Chowdhury, S. Sen, M.I. Islam, M.S. Islam, M.R. Hasan, S. Asaduzzaman, Design of a single-mode photonic crystal fiber with ultra-low material loss and large effective mode area in THz regime, *IET Optoelectronics of Journal* 11 (6) (2017) 265–271.
- [37] J. Liu, H.Q. Liang, B. Liu, X.D. He, Z.P. Chen, Abnormal sensing properties of surface plasmon resonance sensor based on photonic crystal fibers, *Opt. Fiber Technol.* 48 (2019) 248–252.
- [38] S. Sen, S. Chowdhury, K. Ahmed, S. Asaduzzaman, Design of a porous cored hexagonal photonic crystal fiber based optical sensor with high relative sensitivity for lower operating wavelength, *Photonics Sens* 7 (1) (2017) 55–65.
- [39] M.S. Hossain, S. Sen, Design and Performance Improvement of Optical Chemical Sensor Based Photonic Crystal Fiber (PCF) in the Terahertz (THz) Wave Propagation, *Silicon*, 2020, <https://doi.org/10.1007/s12633-020-00696-8>.
- [40] M.I. Islam, K. Ahmed, B.K. Paul, S. Chowdhury, S. Sen, M.S. Islam, S. Asaduzzaman, A.N. Bahar, Ultra-High negative dispersion and nonlinearity-based single mode photonic crystal fiber: design and analysis, *Optics Journal* 48 (1) (2019) 18–25.
- [41] M.S. Hossain, S. Sen, M.M. Hossain, Performance analysis of octagonal photonic crystal fiber (O-PCF) for various communication applications, *Phys. Scripta* 96 (5) (2021) 55506.
- [42] S. Chu, K. Nakkeeran, A.M. Abobaker, S.S. Aphale, P.R. Babu, K. Senthilnathan, Design and analysis of surface-plasmon-resonance-based photonic quasi-crystal fiber biosensor for high-refractive-index liquid analytes, *IEEE J. Sel. Top. Quant. Electron.* 25 (2019) 6900309.
- [43] M.I. Islam, K. Ahmed, M.S. Islam, B.K. Paul, S. Sen, S. Chowdhury, S. Asaduzzaman, A.N. Bahar, M.B.A. Miah, Single-mode spiral shape fiber based liquid sensor with ultra-high and ultra-low loss: design and analysis, *Karbala International Journal of Modern Science* 3 (3) (2017) 131–142.
- [44] Y.D. Liu, X.L. Jing, S.G. Li, S.H. Zhang, Z. Zhang, Y. Guo, J. Wang, S. Wang, High sensitivity surface plasmon resonance sensor based on D-shaped photonic crystal fiber with circular layout, *Opt. Fiber Technol.* 46 (2018) 311–317.
- [45] F. Haider, R.A. Aoni, R. Ahmed, A.E. Miroshnichenko, Highly amplitude-sensitive photonic-crystal-fiber-based plasmonic sensor, *J. Opt. Soc. Am. B* 35 (11) (2018) 2816–2821.
- [46] G. Melwin, K. Senthilnathan, High sensitive D-shaped photonic crystal fiber sensor with V-groove analyte channel, *Optik* 213 (2020) 164779.
- [47] J.J. Lu, L. Yan, Y.H. Han, Y. Liu, J.M. Gao, D-shaped photonic crystal fiber plasmonic refractive index sensor based on gold grating, *Appl. Opt.* 57 (19) (2018) 5268–5272.
- [48] S.X. Jiao, S.F. Gu, H.R. Yang, H.R. Fang, S.B. Xu, Highly sensitive dual-core photonic crystal fiber based on a surface plasmon resonance sensor with a silver nano-continuous grating, *Appl. Opt.* 57 (28) (2018) 8350–8358.
- [49] A.A. Rifat, G.A. Mahdiraji, R. Ahmed, D.M. Chow, Y.M. Sua, Y.G. Shee, F.R. M. Adikan, Copper-graphene-based photonic crystal fiber plasmonic biosensor, *IEEE Photonics J* 8 (1) (2016) 4800408.
- [50] J.N. Dash, R. Das, R. Jha, AZO coated microchannel incorporated PCF based SPR sensor: a numerical analysis, *IEEE Photon. Technol. Lett.* 30 (11) (2018) 1032–1035.
- [51] Q. Liu, J.D. Sun, Y.D. Sun, Z.H. Ren, C. Liu, J.W. Lv, F.M. Wang, L.Y. Wang, W. Liu, T. Sun, P. K Chu, Surface plasmon resonance sensor based on photonic crystal fiber with indium tin oxide film, *Opt. Mater.* 120 (2020) 109800.